Physical seismic modeling of a vertical fault

Jessie M. Arthur, Don C. Lawton, Joe Wong

ABSTRACT

Detecting faults and subsequent deformation zones is significant in geotechnical engineering applications, seismic hazard assessment in earthquake studies, and the petroleum industry for reservoir potential where faults act as a conduit to migrate or trap hydrocarbon flow. Fault identification is also important in shale gas development to design better productive reservoir stimulation by accounting for the slow slip of pre-existing faults during hydraulic fracturing.

This study shows seismic physical modeling results of a shallow vertical fault zone with slight vertical throw. Several physical model prototypes are created with materials which range in velocity and density to best simulate host rock and a deformed fault zone. 2D marine seismic data is acquired and processed at the University of Calgary Seismic Physical Modeling Facility. Physical model materials tested include plaster, sandstone, limestone, lard, wax, and liquid acrylic.

The post-stack imaged results are compared and it can be seen that the fault zone is resolved in both zero offset and common source data from physical modeling. An interesting by-product from the physical modeling acquisition was the identification of ghost reflections captured below the primary reflections, which can be used in ‘mirror imaging’, to provide better illumination of the fault zone.

The modeled fault zone images show a likeness to real 2D seismic data collected over a recent ruptured surface fault in New Zealand.

INTRODUCTION

Detecting shallow fault zones is significant in geotechnical engineering applications and seismic hazard assessment in earthquake studies. The Greendale fault in the Canterbury region of New Zealand was previously undetected when it ruptured the ground surface during the M_w 7.1 Darfield earthquake in 2010. Shallow fault zones can be determined by high resolution seismic reflection profiling (Kaiser et al., 2011), as the deformation of rocks near the fault zone causes changes in lithology, pore pressure, and seismic velocity (Mooney and Ginzburg, 1986).

Fault identification is also important to the petroleum industry, where faults act as a conduit to migrate or trap hydrocarbon flow. However, the effect of faults on a reservoir are complex and difficult to classify as each geologic environment is unique in terms of geometry, distribution, connectivity, and hydraulic properties (Aydin, 2000). A hydrocarbon trap can result from a sealed fault. Reservoirs in direct contact with sheared zones are sealed as a result of accumulated sheared sediment along the fault surface, whereas reservoirs bordering the fault surface are poorly sealed or not sealed (Berg and Avery, 1995). Active faults may act as a conduit to hydrocarbon flow along the fault plane, within the fault zone, and near the tips of active fault zones (Tamagawa and Pollard, 2008).

The identification of fault type is also important in reservoir potential. Improved reservoir performance is seen in areas that have a critically stressed strike-slip fault regime, where high ratios of shear to normal stress produce permeable fracture damage zones along the fault. This is compared to lower reservoir potential in thrust fault stress regimes where fewer fractures with high shear stress ratios exist (Hennings et al., 2012).

Recognition of pre-existing faults is important in shale gas production using hydraulic fracturing to stimulate the reservoir rock. The physical and deformation mechanisms responsible for reservoir stimulation by hydraulic fracturing are complex and not fully understood (Zoback et al., 2012). Microseismic events are an indication of shear slip on faults and fractures caused by hydraulic fracturing used to increase production in unconventional resources. However, production of natural gas generated from hydraulic fracturing does not simply correlate with the number of microseismic events (Vermylen and Zoback, 2011). Recent studies have shown evidence of slow slip, which is indicated by long period, and long duration seismic events on pre-existing fault planes during stimulation, is shown to be a major contributing shear deformation mechanism that creates multiple permeable planes surrounding induced fractures (Das and Zoback, 2011). The need for faults and subsequent deformation zone research is abundant. This study approaches fault detectability by seismic physical modeling, and compares the results to field data acquired transversing the surface ruptured Greendale fault in New Zealand.

Seismic physical modeling provides scaled simulations of real-world scenarios with the benefit of controlled acquisition geometry and physical model properties (Lawton et al., 1998). Modeling of simple faults and geometries are beneficial to understand seismic sections with faults and structure (Angona, 1960). Hilterman (1970) used wood and paper to model synclines, anticlines, and vertical and low angle faults. An electric spark and a condenser microphone served as a source and receiver in this early experiment. Modeled seismic data collected in a water tank has shown success in comparing data processing and imaging between 2D and 3D datasets of ridge and fault models (French, 1974).

Several physical model prototypes of a simple vertical fault which ruptures a geologic surface were created to image a fault deformation zone using 2D marine seismic measurements. The seismic data were acquired at the University of Calgary Seismic Physical modeling Facility which is maintained by the Consortium for Research in Elastic Wave Exploration Seismology (CREWES).

SEISMIC RESOLUTION

Vertical Resolution

The quality of seismic imaging over a fault zone is constrained by seismic resolution. Both vertical and lateral resolution is controlled by spectral bandwidth, and describes the ability to distinguish separate features (Yilmaz, 1987, p. 468). Spectral bandwidth is defined as the standard deviation about the spectral mean, or the center frequency (Barnes, 1993). Dominant wavelength varies with velocity and dominant seismic frequency, and is given by:

$$\lambda = v/f, \tag{1}$$

where λ= wavelength, v= velocity, and f = frequency. Vertical seismic resolution is defined by Widess (1973) as the thickness equal to one eighth of the seismic dominant seismic wavelength. However, one quarter of the predominant wavelength is taken as an industry standard for thin bed vertical resolution as the Widess threshold does not account for noise and wavelet broadening due to attenuation of higher frequencies with depth. Vertical resolution is important in imaging the vertical throw of a fault.

Lateral Resolution

Lateral resolution threshold is determined by the Fresnel zone (Figure 1), an area of constructive reflection accumulation surrounding a reflection point (Lindsey, 1989). The radius of the Fresnel zone is given by the approximation:

$$r \cong \left(\frac{v}{2}\right)\sqrt{\frac{t}{f}} \tag{2}$$

where r= radius of the Fresnel zone, v= velocity, t=time, f= frequency. Two reflecting points that fall within the Fresnel zone are considered irresolvable, therefore lateral resolution improves as the Fresnel zone narrows. The deformation zone of shallower faults is more resolvable than deeper faults, as the Fresnel zone increases in area with depth.

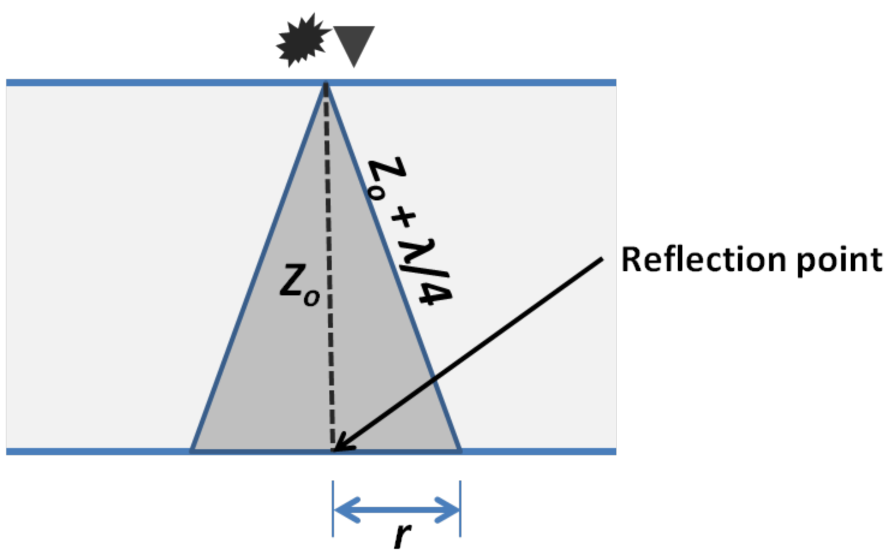

FIG. 1. The Fresnel zone radius (r) for a coincident source and receiver. Adapted from Yilmaz (1987).

PHYSICAL MODELING

The physical models

The displacement and deformation zone of the Greendale fault, which was ruptured during the 2010 Darfield earthquake, served as a general guide in creating the fault models. The Greendale fault surface rupture was mainly dextral strike-slip with 2.5 m average displacement, vertical displacement less than 0.75 m, and a 30 to 300 m wide deformation zone (Van Dissen et al., 2011). Pure strike slip faults are difficult to detect in seismic imaging due to lack of significant vertical displacement (Fossen, 2010, p.356). However, deformed bends associated with strike-slip faults may split and widen upward into flower structures, which may be more detectable in seismic imaging as there is a wider fault zone in the near surface. Fault zones also show reduced seismic velocities which are associated with densely cracked and fractured rocks, altered rock composition, and near-surface fault gouge material (Mooney and Ginzburg, 1986).

Given these considerations, several physical model prototypes were constructed to best represent a vertical fault that ruptures the surface. A fault zone was created, closed at one end of the model fault length, and widens with fault length distance. Several types of materials are used to create the models and are summarized in Table 1. The velocities of the materials were measured with a Tektronix TDS 420A 200 MHz 4 Channel Digital Real-Time Oscilloscope. All of the models had 2D zero-offset seismic reflection surveys acquired as a quality check. Survey parameters are discussed in greater detail in the next section.

Table 1. Summary of physical model prototypes

	Model 1		Model 2		Model 3		Model 4		Model 5	
	Model material	Fault zone infill	Model material	Fault zone infill	Model material	Fault zone infill	Model material	Fault zone infill	Model material	Fault zone infill
	Plaster of Paris	Lard	Sandstone	Epoxy	Limestone	Wax	Limestone	Water	Limestone	Liquid Acrylic
Density (g/cm^3)	1.3	0.98	2.6	1.7	2.9	1.1	2.9	1.0	2.9	1.2
Measured Velocity (m/s)	2035	1490	2965	2680	5100	1510	5100	1480	5100	2460

The model and seismic acquisition measurements are scaled, where 1 mm in the physical modeling world is equivalent to 10 m in field equivalents (1:10000). Ultrasonic modeling frequencies of 100 kHz to 1,000 kHz are scaled down by the scaling factor of 10,000 to represent real-world seismic frequencies of 10 Hz to 100 Hz. All referred measurements are scaled to represent field values and measurements have an approximate error of 5%.

The Plaster of Paris-Lard model (Model 1) has an average thickness of 285 m. Issues arose with this model due to air bubbles setting in the plaster as it dried, and the lifespan of the model was limited as the seismic surveys were acquired in water. The Sandstone-Epoxy model (Model 2) has an average thickness of 248 m and one side was uplifted by 30 m. The epoxy had set too quickly and only a constant width fault gap width of 30 m was created. An additional model was created with Portland cement using coarse grained sand. The model was sturdy; however scaled grain sizes of the rock would be equivalent to 5 m. These unrealistic grain sizes contribute to point scattering in a seismic reflection survey. The limestone model (Model 5) with an average thickness of 300 m, showed greatest promise as potential modeling material.

Different fault-zone infill materials were tested: water, lard, wax, epoxy, and finally acrylic plastic. A material was sought which had a higher velocity than paraffin wax and lard, which was close to the velocity of water. The epoxy used with the sandstone had a higher velocity of 2680 m/s, however, it set much too quickly, making it difficult to work with. The final fault infill material selected was a liquid acrylic (2460 m/s) which sets to a hard resin. The limestone model was fixed in place with putty, and sealed with wax to prevent leakage. The model was also uplifted on one side by approximately 10 m. At this point in the study, the limestone models with both a water-filled and acrylic-filled fault zone were considered optimal, and the results are compared in further analysis.

Physical modeling data acquisition

The University of Calgary Seismic Physical Modeling Facility supports both acoustic and elastic modeling. For this study, only the acoustic modeling is considered. Dynasen Inc. CA1136-12 piezoelectric pin transducers (305mm long and 24mm diameter) acting as an acoustic source and receiver are carried in a carriage attached to a beam which moves along aluminum tracks. The transducers produce and detect vibrations with particle motion in the vertical direction (Wong et al., 2011). The modeling systems are described in further detail by Cheadle et al. (1985), Lawton et al. (1989), Gallant et al. (1991), and Wong et al. (2009a).

The physical models were immersed in a water tank for seismic acquisition modeling. Each model was placed on top of an aluminum plate, which rested on a phenolic resin block. A schematic of the Limestone model in the tank is shown in Figure 2. The models were placed in the tank with the fault length parallel to the N-S direction of the room, representing the x-axis, with the thinner end of the fault in the positive x-axis direction (Figure 3). A zero-marker was placed on all the models for coordinate reference and was located approximately 120 m East of the fault (Y=+120).

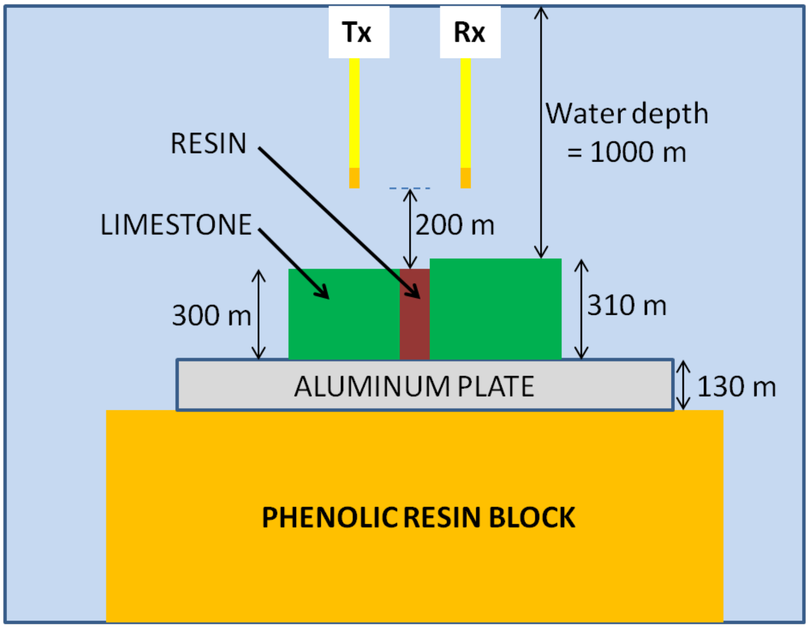

FIG. 2. Schematic diagram of seismic acquisition over the final limestone model with corresponding field dimensions. The transducers are positioned 200 m over the model.

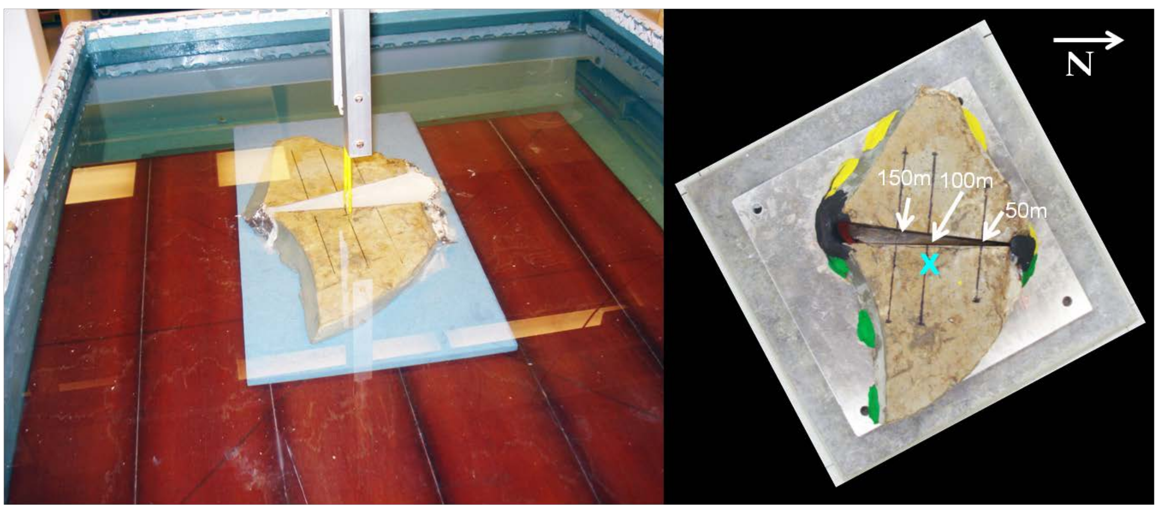

FIG. 3. The Limestone-Wax model in the physical modeling water tank (left), and the limestone model (right), held in place by putty prior to fault zone infill. The blue 'x' signifies the zero marker location.

A zero-offset section, acquired by a coincident source and receiver which step along the seismic profile, was acquired for quality control of all the models to determine suitability for further investigation. Although the transducers were not exactly coincident due to the carriages, they are near-offset, with a spacing of 5 mm (50 m, scaled), and the data are processed assuming a coincident source and receiver. The zero-offset profiles ran perpendicular to the fault length along the y-axis, with the transmitter-receiver pair moving in 5 m increments with a 50-m offset in line with the fault (Figure 4). Three profiles were collected over each model at varying fault zone thicknesses. For the final limestone models, the surveys ran from Y=-700 to Y=+900 (321 traces), and crossed fault zone widths of 50, 100, and 150 metres.

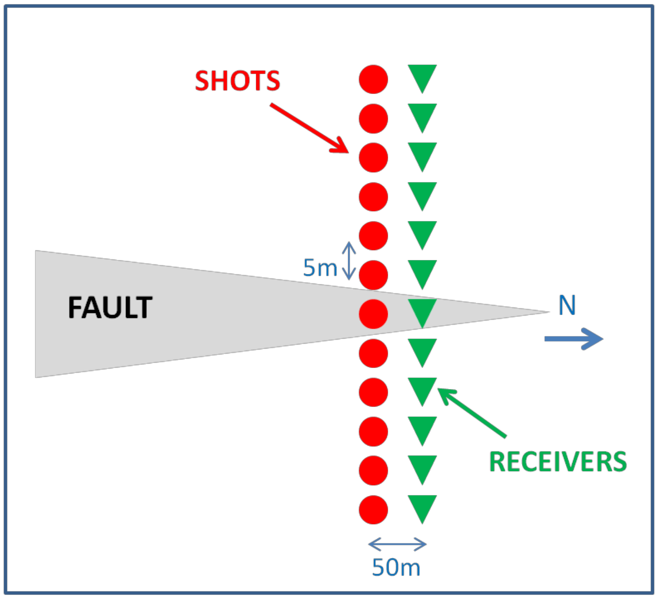

FIG. 4. Plan view of the zero-offset acquisition. The Tx-Rx pair moved in 5 m increments and have 50 m offset.

Common-source gathers were acquired for the Limestone models over the 50 m fault width. The survey for the Limestone models ran from Y=-300 to Y=+700. The source increment spacing was 10 m, and 101 shots were collected perpendicular across the fault length. The receiver spacing was 5 m and 201 traces were collected in each shot gather. The maximum fold was 101. A sample rate of 1 ms (scaled units) was used during all acquisition. For comparison with the common-source data, only the zero-offset data from the 50 m fault gap will be discussed.

SEISMIC DATA PROCESSING

The seismic data was initially viewed in Seisee for quality control, and then processed in GEDCO's VISTA seismic data processing software. Two processing flows were developed: a processing flow for the zero-offset data, and a flow for the common-source data. The flows created in VISTA are shown Appendix A. A general description of the processing flows is discussed in this section; however, there may have been some modification in processing parameters to best fit each dataset.

Zero-offset data processing

A zero offset time section provides an image of data traces which have an equivalent source-to-geophone distance. In this case, the offset distance is 5 mm (or 50 m, scaled) and the source-receiver pair increment is 0.5 mm (5 m, scaled). The benefit of acquiring zero offset data is that minimal processing is required to obtain an image of the subsurface. The general processing flow used to image the zero offset data is given in Figure 5, with the goal of providing a clear image of the surface fault. To illustrate examples, this discussion will be limited to the top 1 s of the Limestone-Acrylic model data.

1. Top Mute
2. Spiking Deconvolution
3. Mean Scaling
4. FK Filter
5. Mean Scaling
6. 2D Kirchhoff migration
7. AGC and Bandpass

FIG 5. General processing flow applied to the zero-offset data.

The raw image of the zero-offset time section, with 321 traces, is shown in Figure 6. After performing filter panel tests, a wide bandpass filter of 5-10-80-90 Hz was initially applied followed by spiking deconvolution. Spiking deconvolution shortens the period of the embedded source wavelet, trying to create a spike (Geldart and Sheriff, 2004). Autocorrelation of the deconvolved data was examined for operator lengths of 20, 40, and 60 ms (Figure 7). The operator length of 60 ms was chosen, since reverberations in the data are suppressed, and the limestone bottom expected at ~420 ms becomes detectable. The deconvolved data with the tested operator lengths are shown in Figure 8. The operator was designed on a 200 to 1000 ms time gate. Predictive deconvolution was also investigated; however it seemed to best repress the reverberations in the much later multiples. At this time, the goal remains to focus on the primary reflection data.

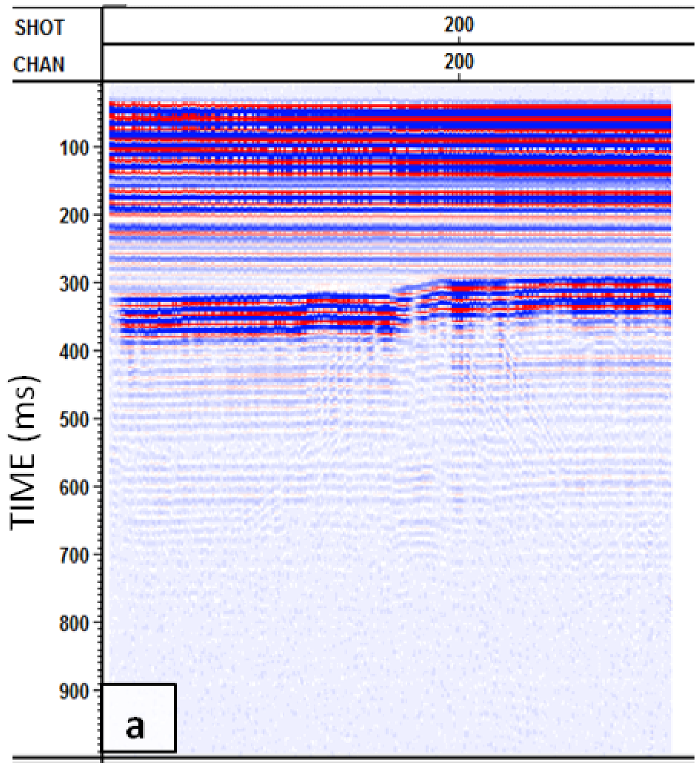

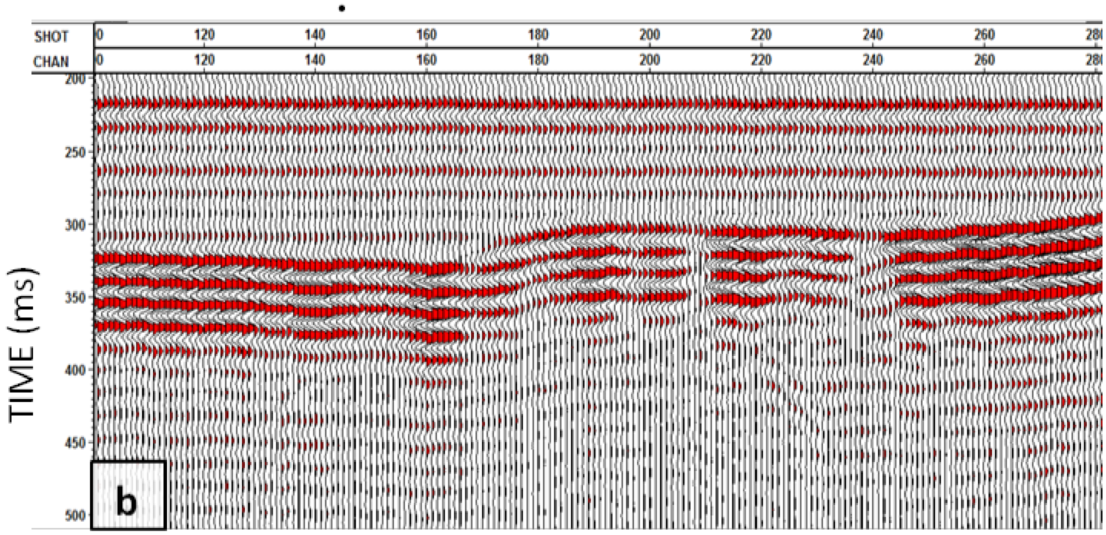

FIG. 6. a) Raw image of the zero-offset seismic data. b) Zoomed wiggle trace of fault zone.

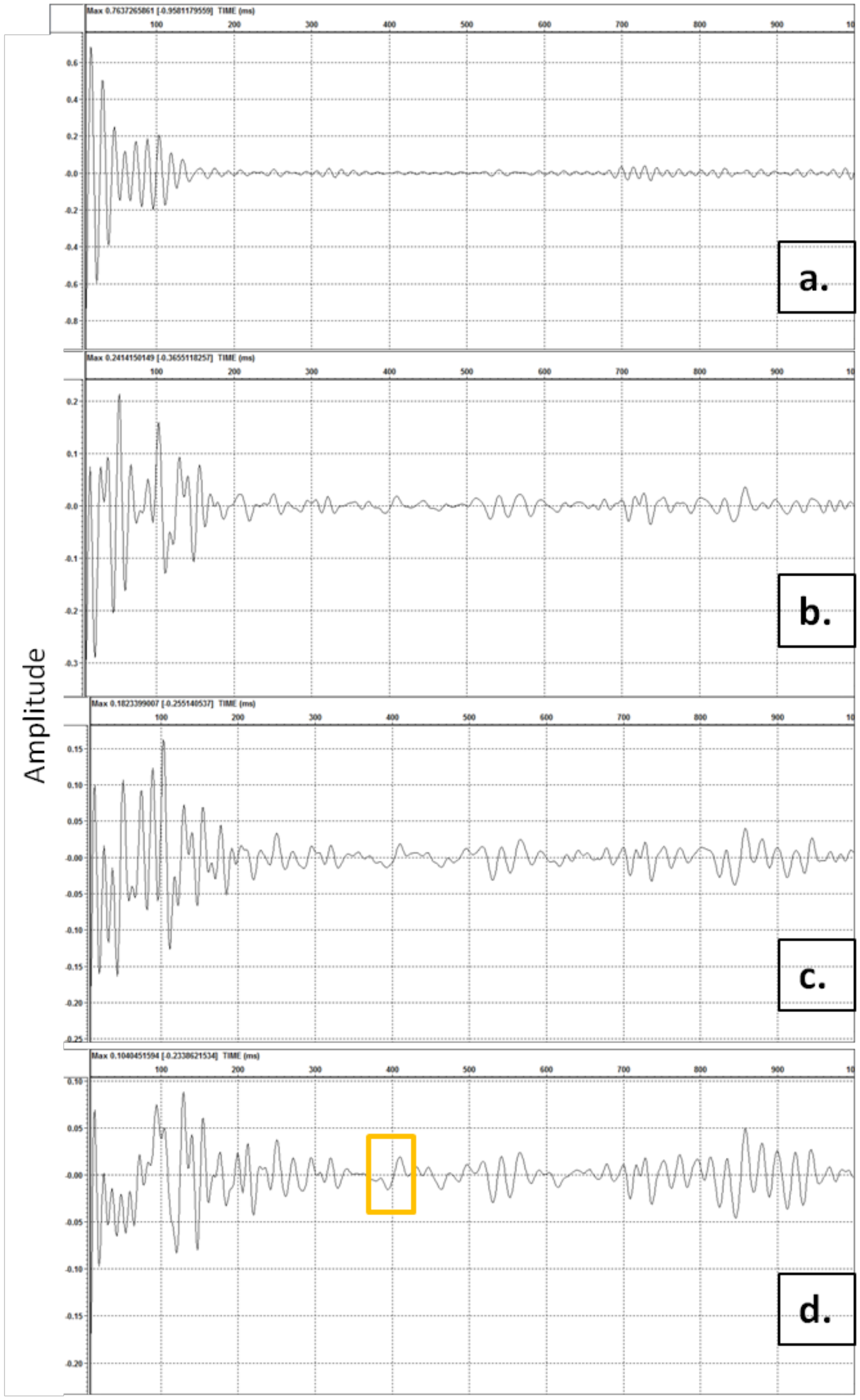

FIG. 7. Autocorrelation of the deconvolved data was examined. a) Raw data. Operator lengths of b) 20, c) 40, and d) 60 ms. The yellow box highlights the signal of the bottom of the limestone model.

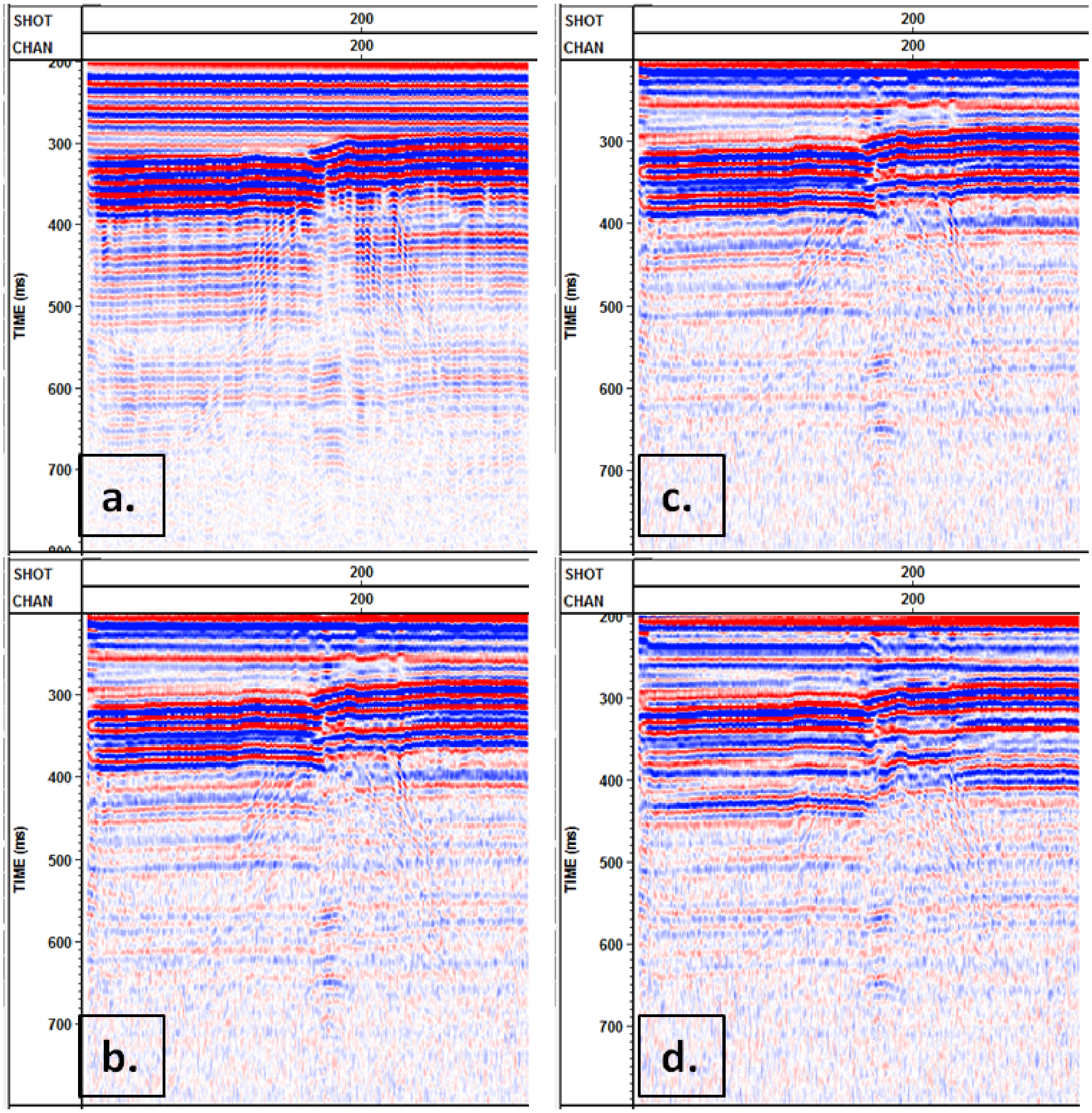

FIG. 8. a) Raw data. The deconvolved data with tested operator lengths of b) 20 ms, c) 40 ms, and d) 60 ms.

Prior to migration, random noise and increased noise from spiking deconvolution was attenuated in the FK domain with a symmetrical fan filter (Figure 9). The migrated data were imaged with a 2D Kirchhoff time migration algorithm with a maximum lateral migration operator (or aperture) of 10 traces. In order to image true reflection amplitude, the migration aperture must be larger than the Fresnel zone (Sun and Bancroft, 2001). Comparisons of the final migrated image with tested migration apertures are shown in Figure 10. A minimum aperture was selected for the final image to agree with the approximated calculation of a Fresnel zone of 25 m. A constant velocity of water (1480 m/s) was used in the migration algorithm. Scaling (AGC) and bandpass filtering were applied to the final migrated images for viewing.

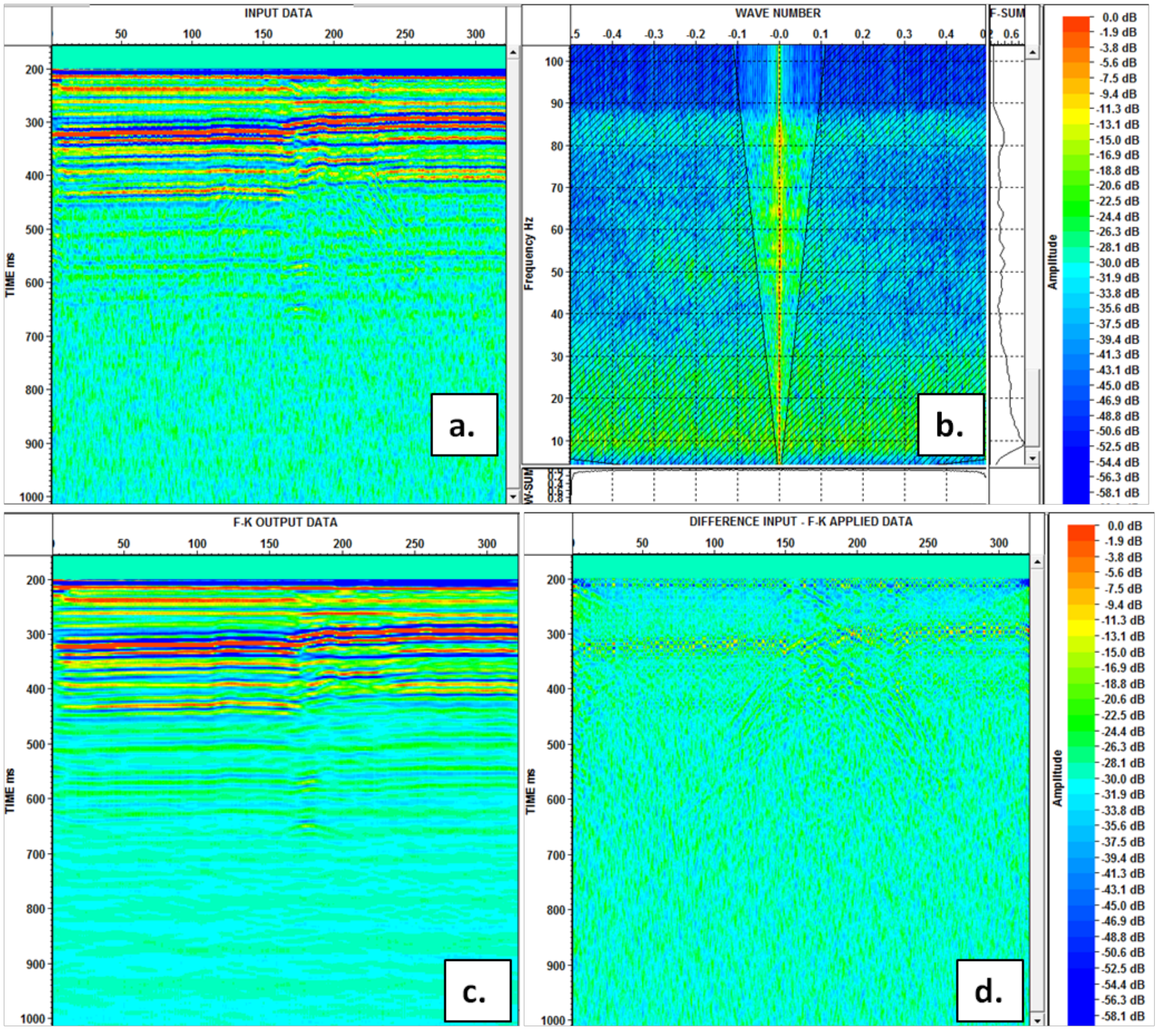

FIG. 9. Noise attenuated in the FK domain with a symmetrical fan filter. a) Input, b) Applied filter, c) Output, d) Noise removed.

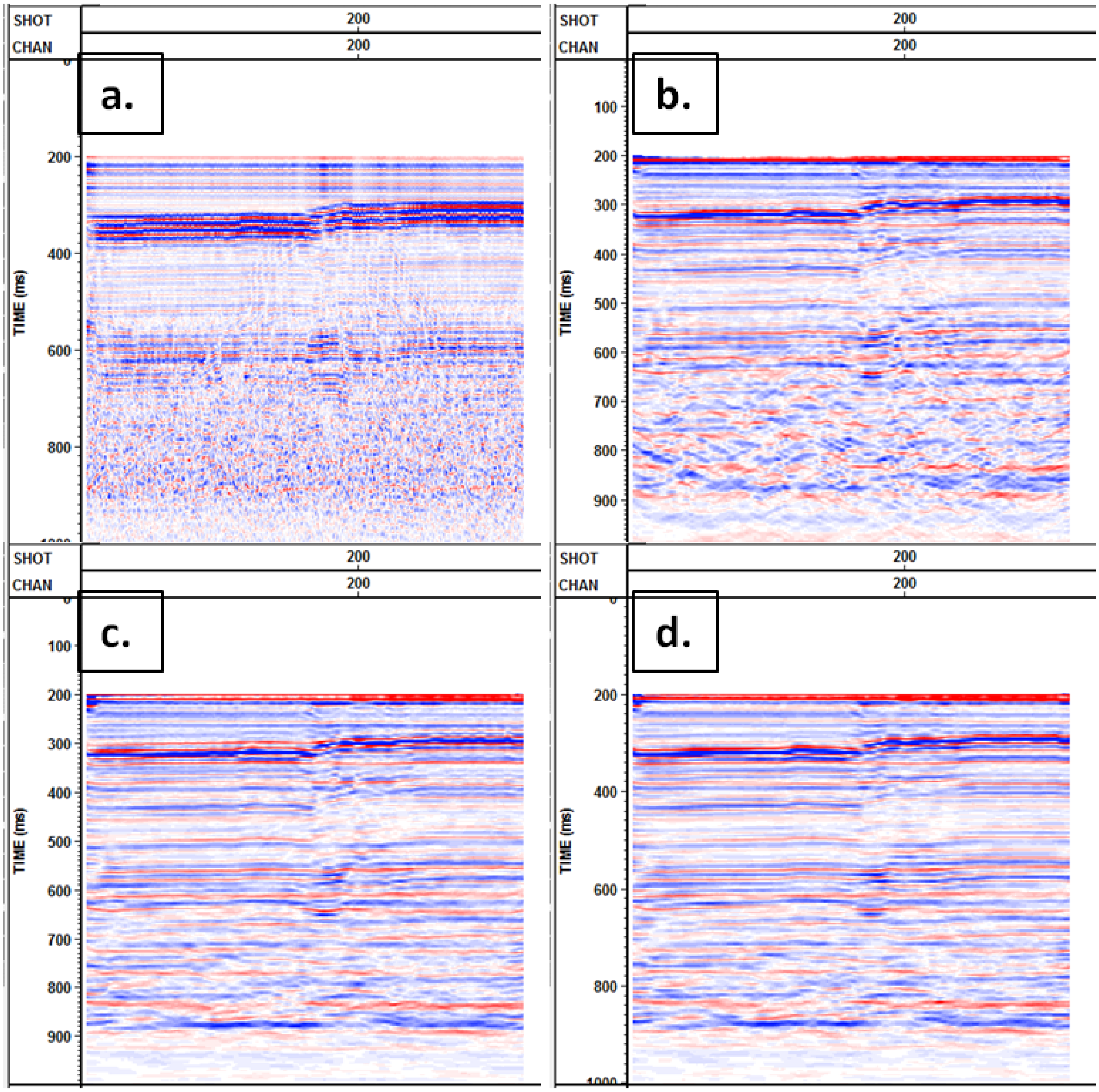

FIG. 10. Comparisons of the final 2D Kirchhoff migrated image with tested migration apertures. a) Raw and scale data, b) Migration aperture = 50 traces, c) Migration aperture = 15 traces, d) Selected migration aperture = 10 traces.

Common source data processing

The general processing flow for the common-shot data is given in Figure 11, which was applied to the Limestone-Water and Limestone-Acrylic fault models. The processing sequence involves sorting and creating geometry, denoising in shot domain, velocity analysis and NMO, stack, and migration.

1. Geometry
2. Top Mute
3. Bandpass filter
4. FK Filter
5. Exponential Time Power Gain
6. Spiking Deconvolution
7. Mean Scaling & Filter
8. Velocity Analysis
9. NMO & Stretch Mute
10. Stack
11. FK Filter
12. Kirchhoff Migration
13. AGC & Filter

FIG. 11. General processing flow applied to the common-source data.

The survey geometry was loaded from trace headers, and some edits were applied to ensure the data were in sequential order. Midpoint coordinates and offset vectors were created and saved to the geometry. A conservative surgical top mute was applied to mute the energy of the direct wave.

An average trace calculation was applied on the raw data to investigate the frequency content in an amplitude spectrum (Figure 12). Throughout the data, two energy bands are visible in the amplitude spectrum between 30 – 45 Hz and 50-75 Hz. For this dataset, the signal is estimated to be in the higher frequency band, with a dominant frequency of approximately 60 Hz. Further investigation is needed to determine if the two-banded amplitude spectrum is common in this type of seismic modeling data.

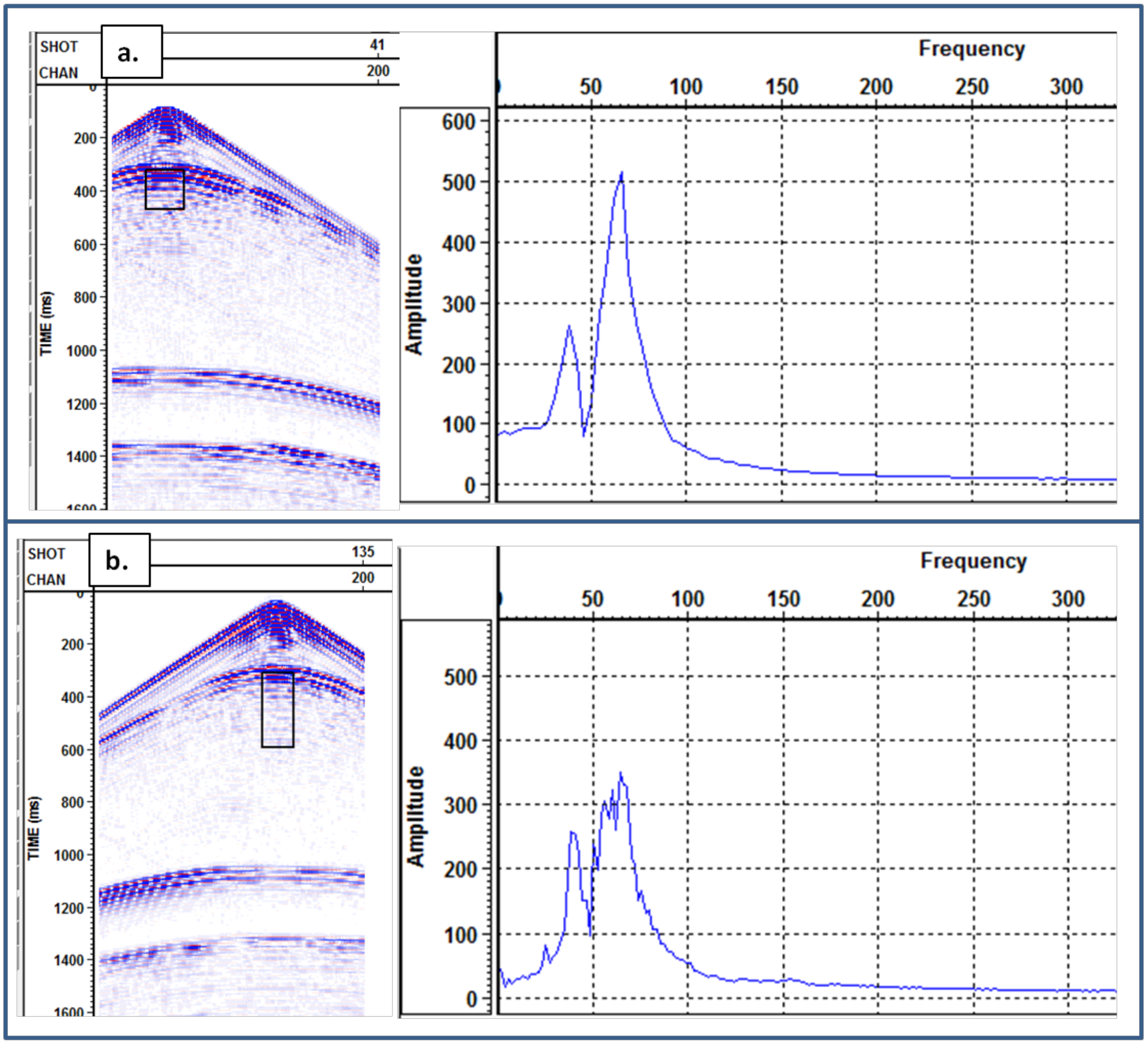

FIG 12. Spectral analysis of a) SP 41 of the Limestone-Acrylic model, and b) SP 135 of the Limestone-Water model. Two bands of energy are apparent throughout the data.

While in the shot domain, an FK filter was applied to remove random noise, and more energy from the direct wave (Figure 13). An exponential time power function of 1.4 was then applied to gain the data.

Spiking deconvolution was applied with a 20 ms operator, 10 ms taper, and 1% prewhitening. Operator lengths of 20, 40, 90, and 120 ms were tested (Figure 14). A comparison of the pre- and post- deconvolved shot point 101 for the Limestone-Acrylic model is shown in Figure 15. Mean scaling was then applied to whiten the spectrum of the data, and a bandpass filter of 5-10-80-90 Hz was applied.

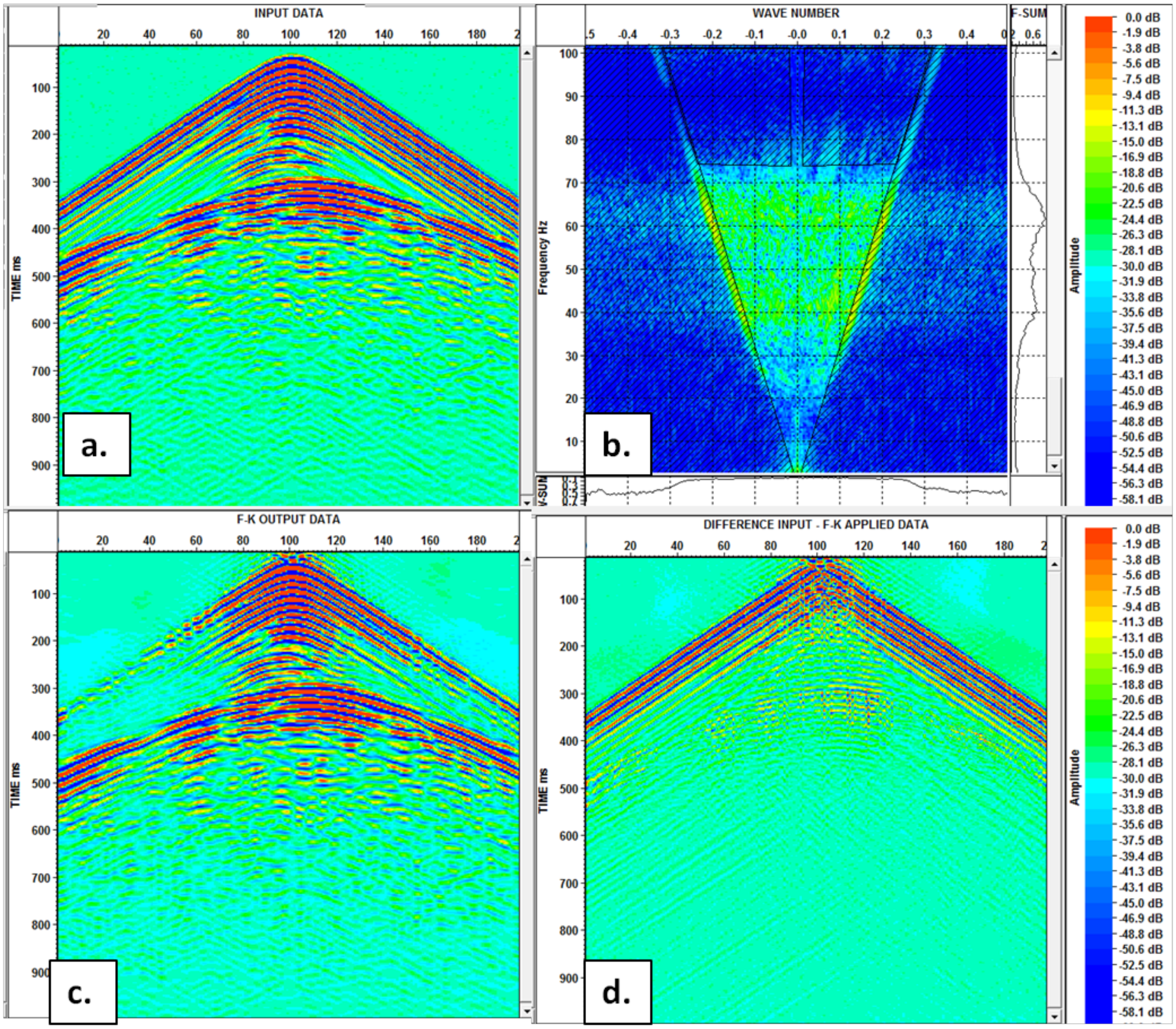

FIG. 13. Noise attenuated in the FK domain with a symmetrical fan filter on the Limestone-Acrylic model in the shot domain. a) Input, b) Applied filter, c) Output, d) Noise removed.

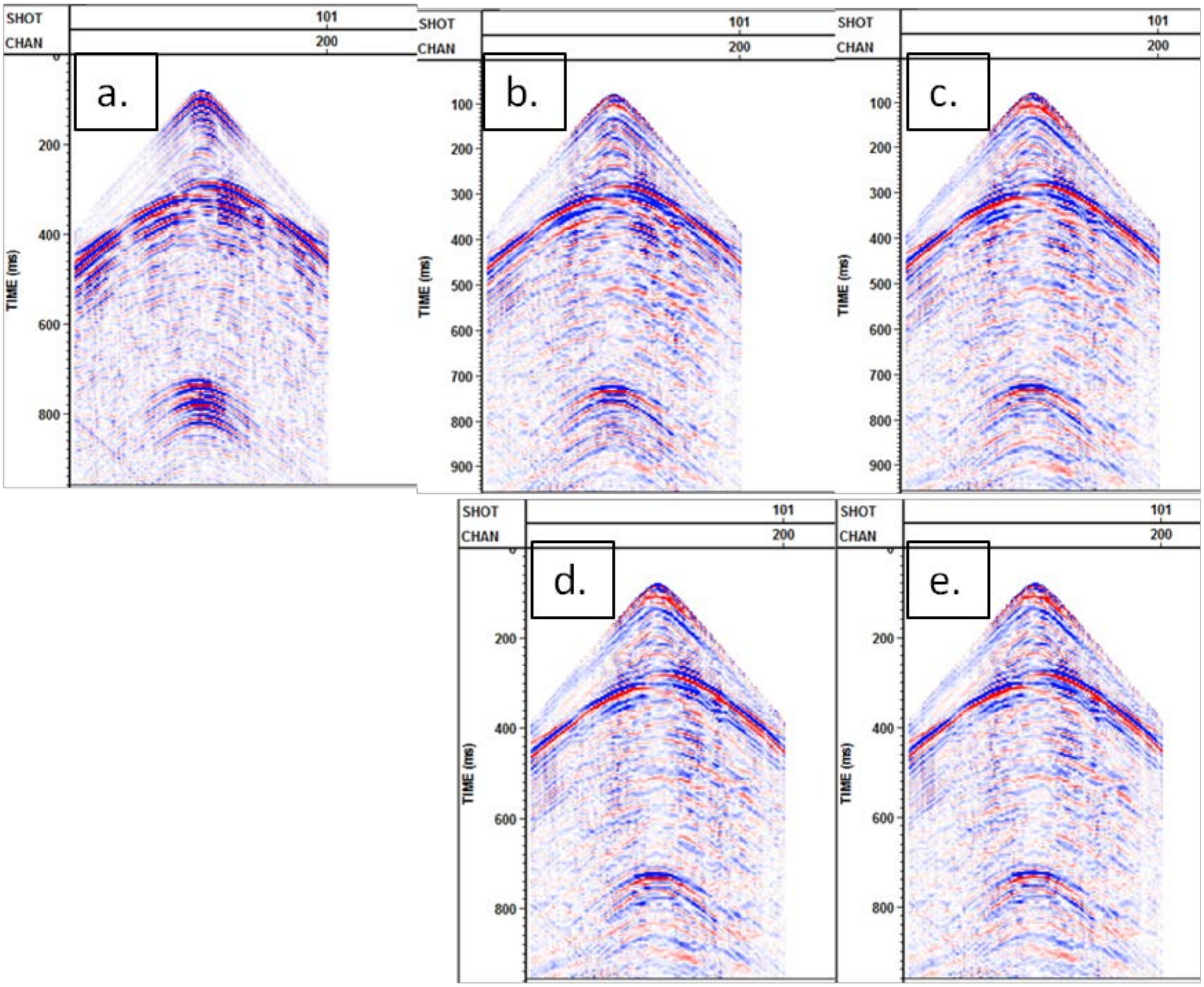

FIG. 14. Spiking deconvolution testing on SP 101 of the Limestone-Water fault model. a) Raw shot, b) Operator length = 20, c) = 40, d) = 90, and e) = 120 ms. The 20 ms operator length was selected.

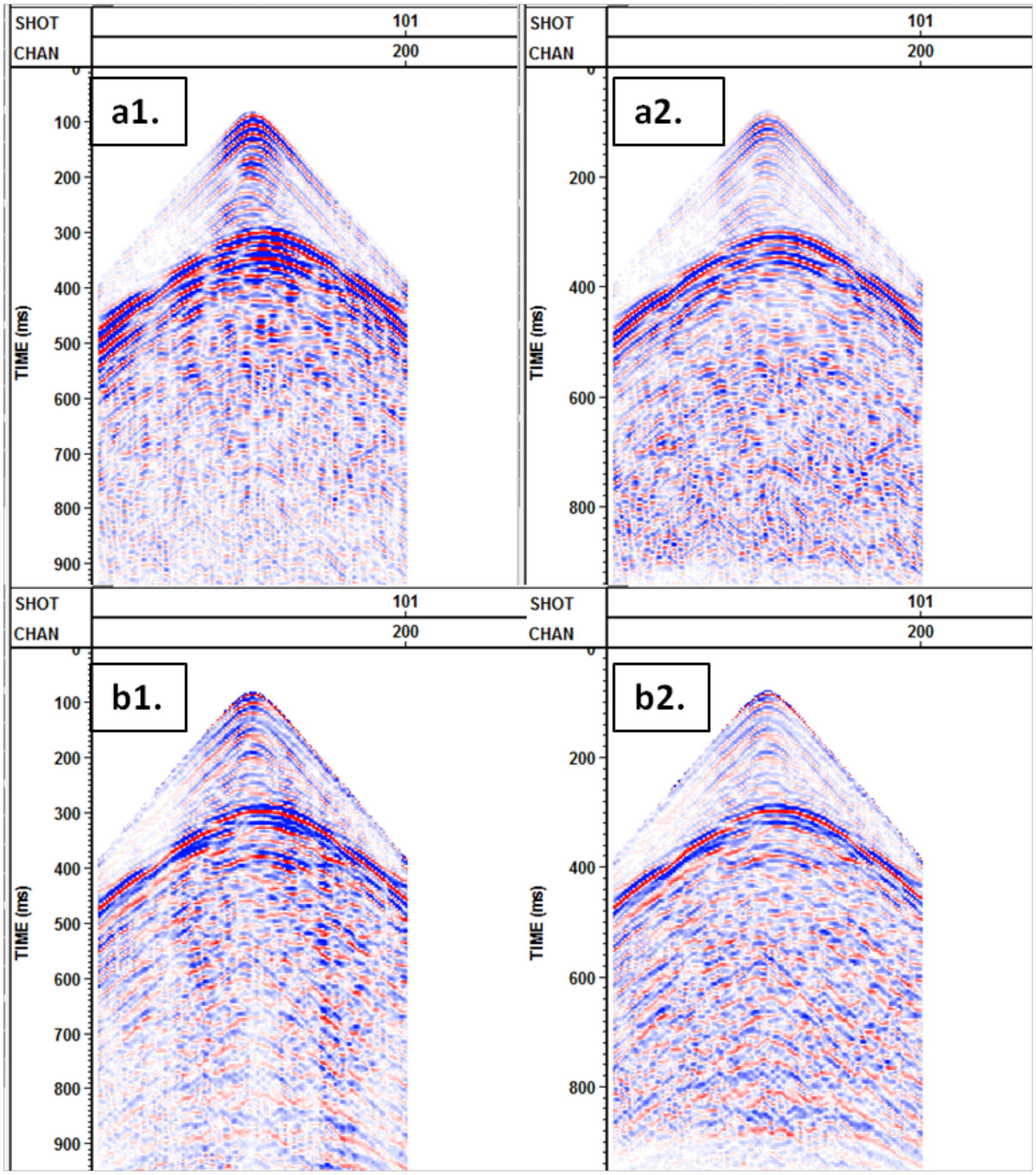

FIG. 15. A comparison of the pre- and post- deconvolved SP 101 for the Limestone-Acrylic model. FK-Filter and ExpTPower is applied. a1) No decon, AmpSc=8, a2) With decon (operator = 20 ms), ampsc=8. b1 & b2 are the same, but have AGC applied.

Velocity analysis was performed on CMP sorted seismic data to correct for non-zero offsets. Normal moveout (NMO) is the time difference between travel time at zero-offset and a given offset (Yilmaz, 1987, p.155). A supergather of 5 CMP bins per zone was created, and used in semblance analysis. Borrowing traces from nearby midpoints increases signal to noise ratio, and keeping a small mix of CMP gathers ensures resolution is not compromised. Semblance and constant velocity stack analysis was performed on every tenth CMP. The velocity picks at CMP 201, which is where the center of the fault is located, is shown in Figure 16 for both the Limestone-Acrylic and Limestone-Water models. A mute was picked on every tenth CMP to cut moveout stretch at far offsets. The final velocity models are shown in Figure 17. The velocity models are similar; however, a decrease in velocity is seen in the water filled fault compared to the acrylic filled fault, as expected. The CMP gathers are NMO corrected and the picked stretch mute is applied. All data found within a CMP bin is then compressed to form a stacked section (Figure 18).

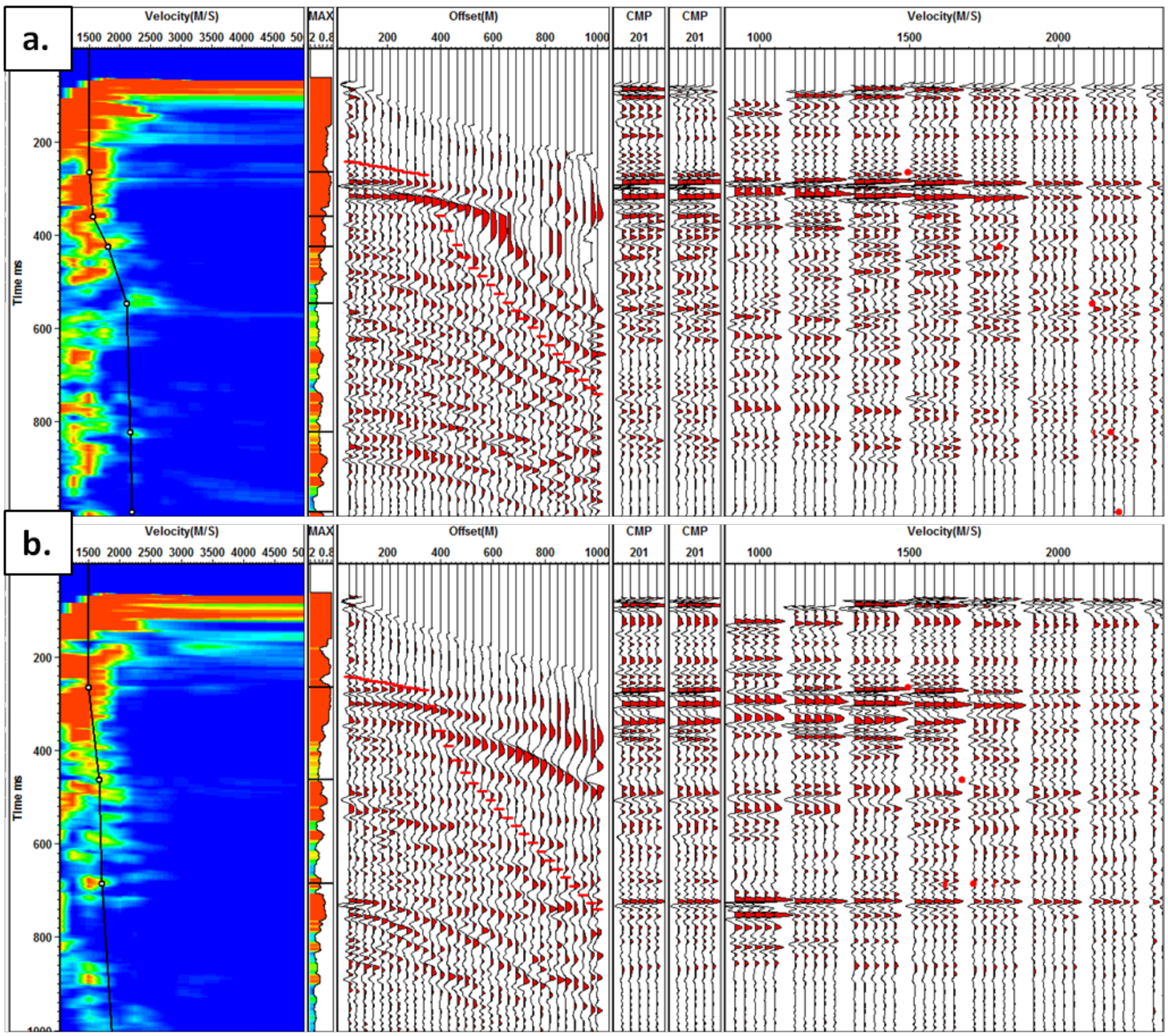

FIG. 16. Semblance and constant velocity stack analysis for a) the Limestone-Acrylic model, and b) the Limestone-Water model. The velocity picks at CMP 201, which is where the center of the fault is located. The velocities and a mute function were picked on every tenth CMP.

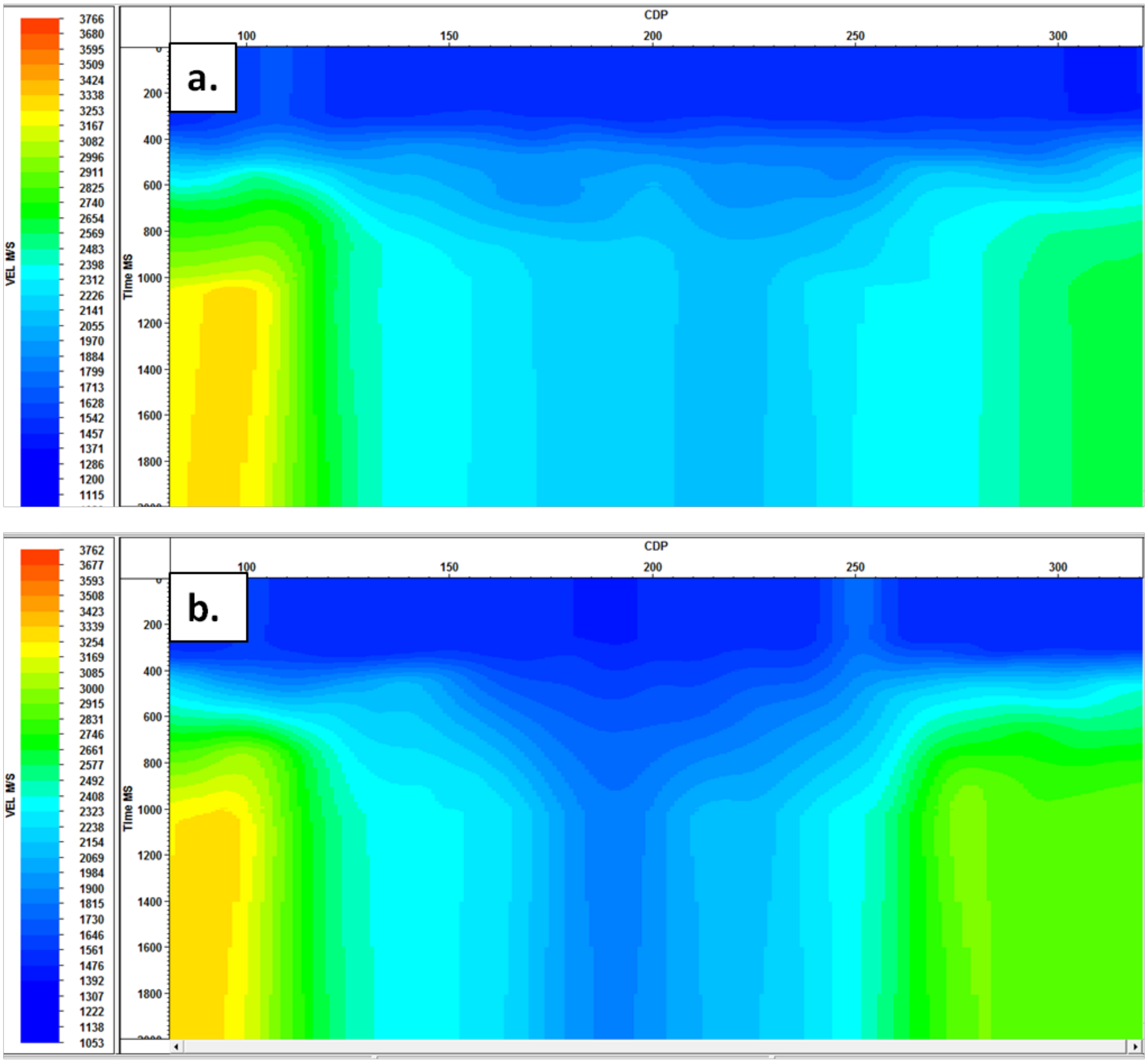

FIG. 17. The final velocity models for a) the Limestone-Acrylic model, and b) the Limestone-Water model. A decrease in velocity is seen in the water filled fault compared to the acrylic filled fault.

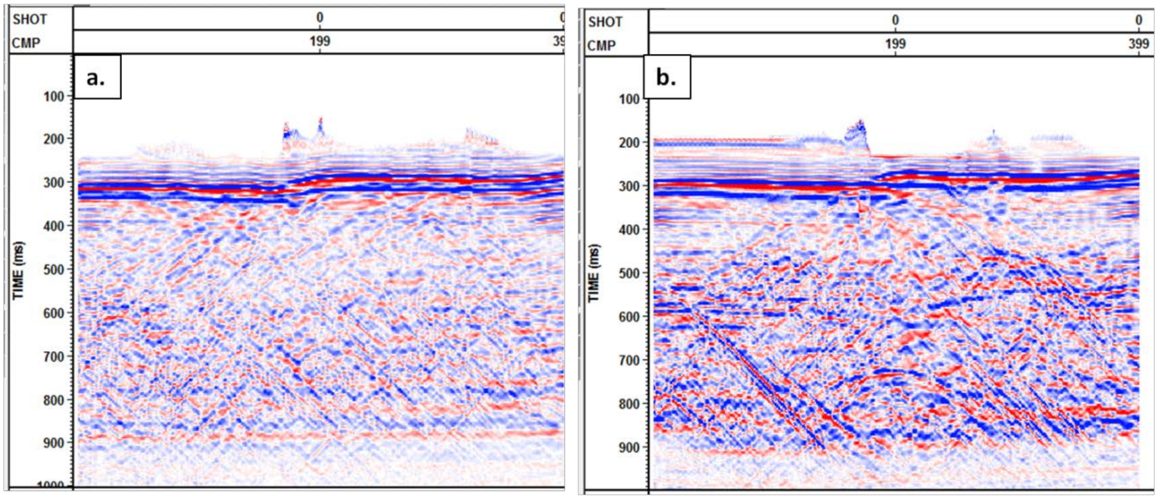

FIG. 18. a) Stacked seismic section of the Limestone-Acrylic fault model, b) Stack of the Limestone-Water fault model.

An additional pass of FK fan filtering was applied to the stacked section of both models in order to remove what appears to be diagonal linear noise, which is much more apparent in the Limestone-Water fault model between 600-900 ms. A possible interpretation of this more prominent linear feature in the Limestone-Water fault model is sideswipe, defined by Sheriff (2002) as "evidence of a structure feature which lies off to the side". This noise was observed in the shot domain as well, however, it is easily removed from the stacked section in the FK domain (Figure 19).

A 2D poststack Kirchhoff time migration algorithm was applied to the CMP stack data volumes. The goal of migration is to collapse diffractions, and move reflectors to their actual subsurface positions to make the stacked section more similar to the geologic cross section along the seismic line (Yilmaz, 1987, p.241). The migration operator parameters for the common source data sets is the same as the zero offset data sets, as the CMP stack is equivalent to a zero offset section. A final flat top mute of 200 ms was applied, with an AGC window length of 300ms and bandpass filtering for viewing (Figure 20).

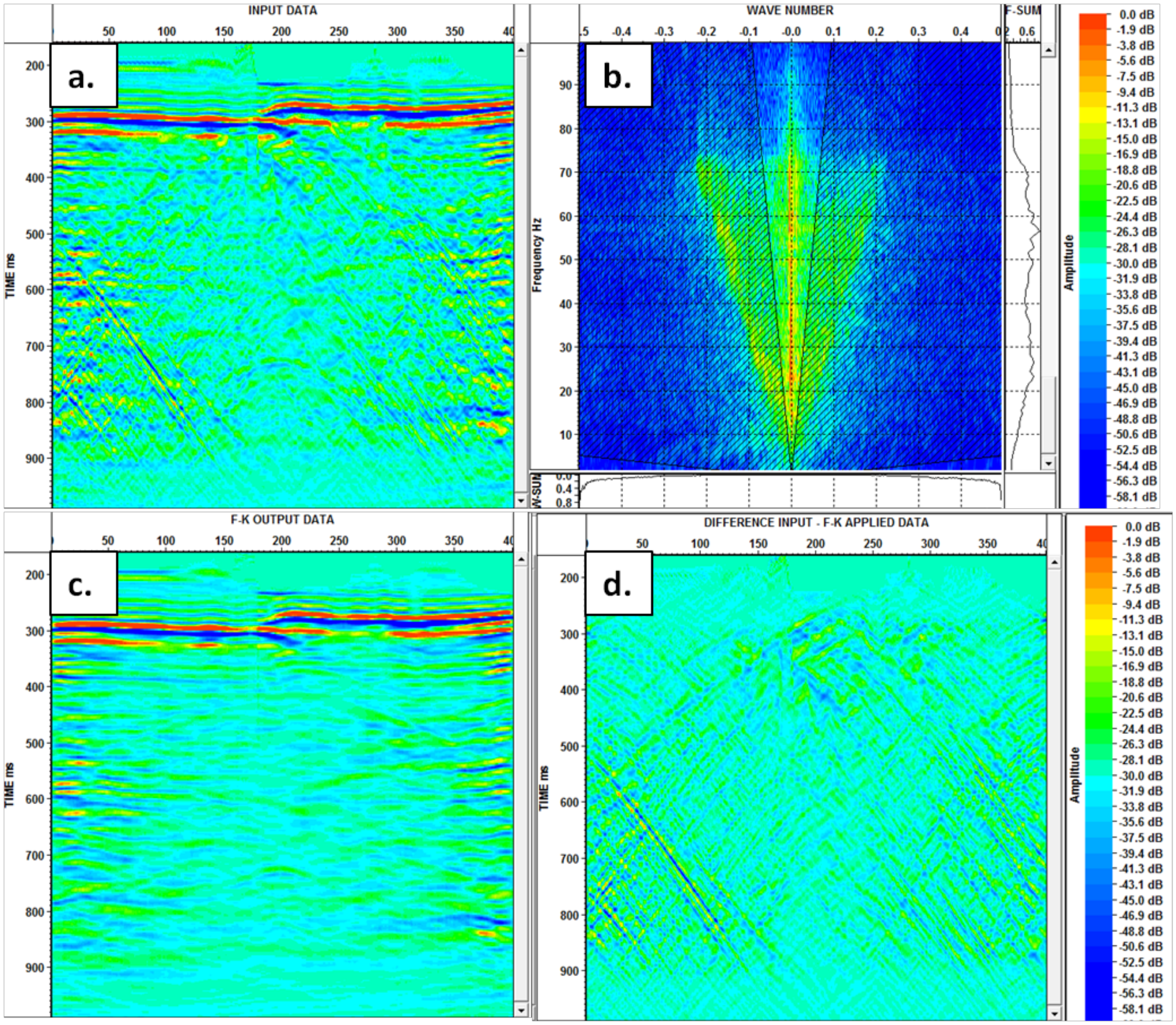

FIG. 19. Noise attenuated in the FK domain with a symmetrical fan filter on the Limestone-Water model CMP stack. a) Input, b) Applied filter, c) Output, d) Noise removed.

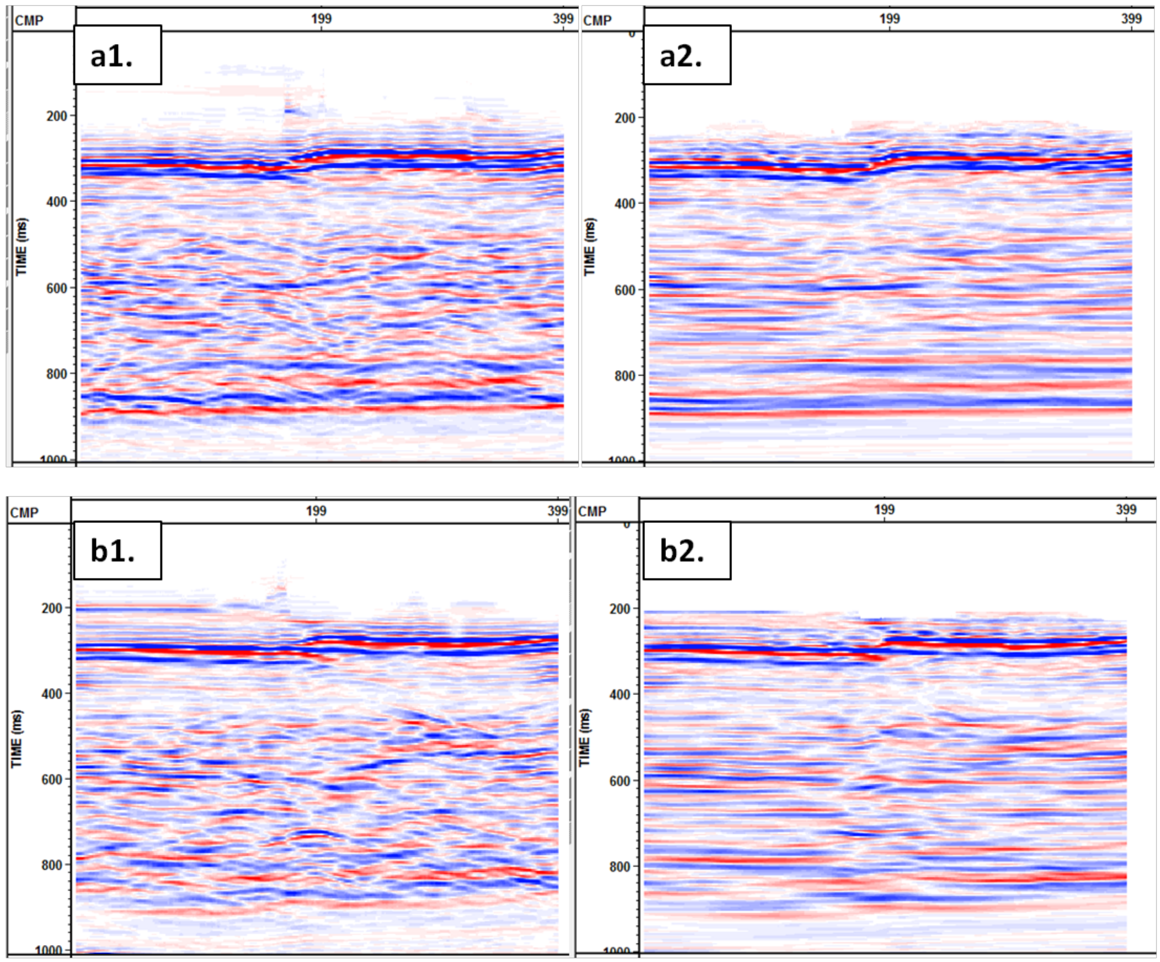

FIG. 20. a1) CMP stack of the Limestone-Acrylic fault model, followed by a2) Poststack migration. b1) CMP stack of the Limestone-Water fault model, followed by b2) Poststack migration.

EVENT IDENTIFICATION

Event identification by arrival times in the processed results was done by raytracing, which assumes the raypaths obey Snell's law and velocities are known (Sheriff, 1991, p. 242). Reflection events are labeled on raw shot 101 of the Limestone-Water common source model (Figure 21). An average trace calculation shows the events more clearly for the same shot record (Figure 22). The events were identified by calculating the two-way travel times, for primary and multiple reflections. Figure 23 illustrates the ray paths taken of each labeled event, and the summary of expected two-way time which the events are located is given in Table 2. The expected time is approximate, and small errors result from measurement of limestone thickness, water depth measurement and evaporation over time in the tank, and the assumption that the model is perfectly homogeneous. Down going events (Event E and F) are ghosts, while the other events listed are up going primaries.

The ghost reflections identified are interesting as they do not interfere with the primary upgoing reflections for this dataset, and may be useful in further imaging as an additional topic. When the water surface acts as a mirror reflecting the subsurface, 'mirror imaging' uses receiver ghosts (Grion et al., 2007). In fact, multiples can be imaged separately from primaries to provide a better illumination of the subsurface (Wang et al., 2012).

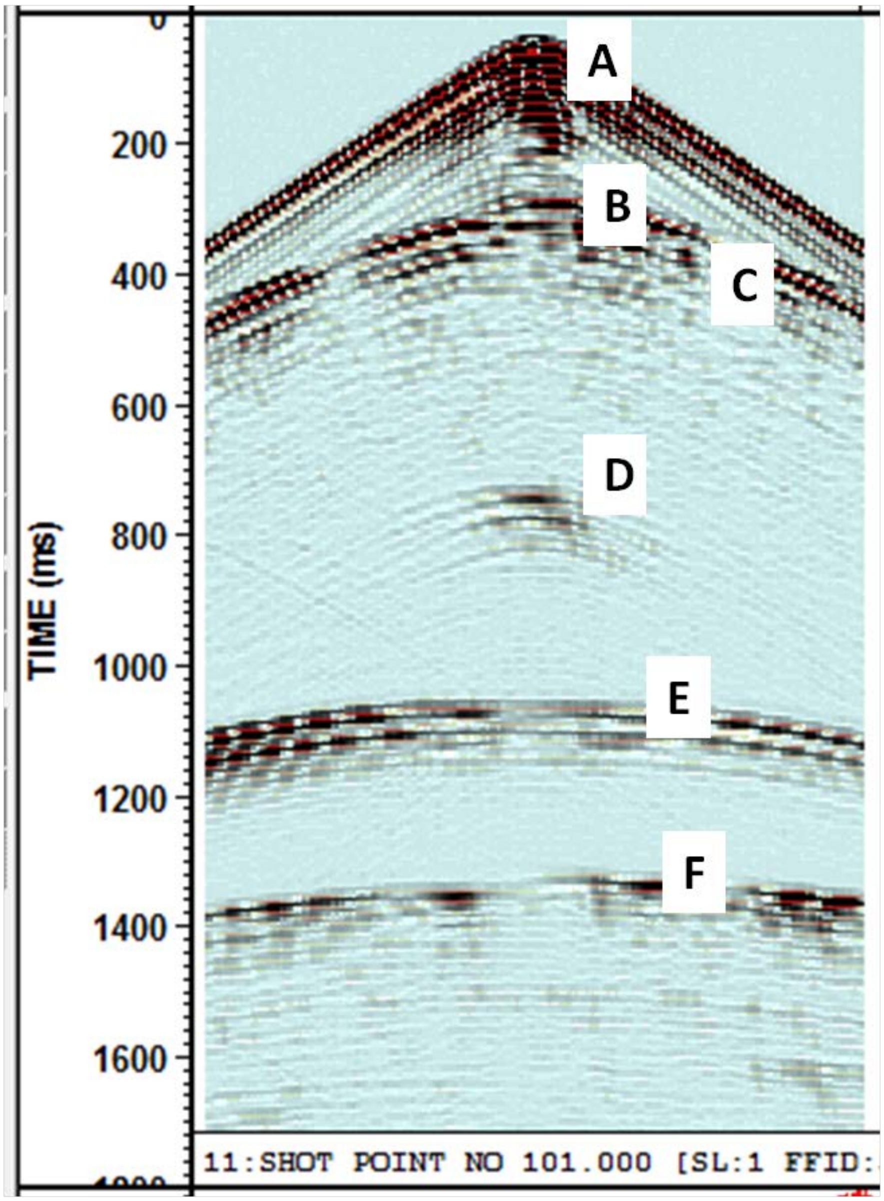

FIG. 21. Event identification by ray tracing. A: Direct arrival (~32 ms), B: Water bottom/top of fault (~270 ms), C: Bottom of limestone (~380-400 ms), D: Bottom of water filled fault (~720 ms), E: Source ghost (~1020 ms), F: Receiver ghost/multiple of water bottom (~1275 ms).

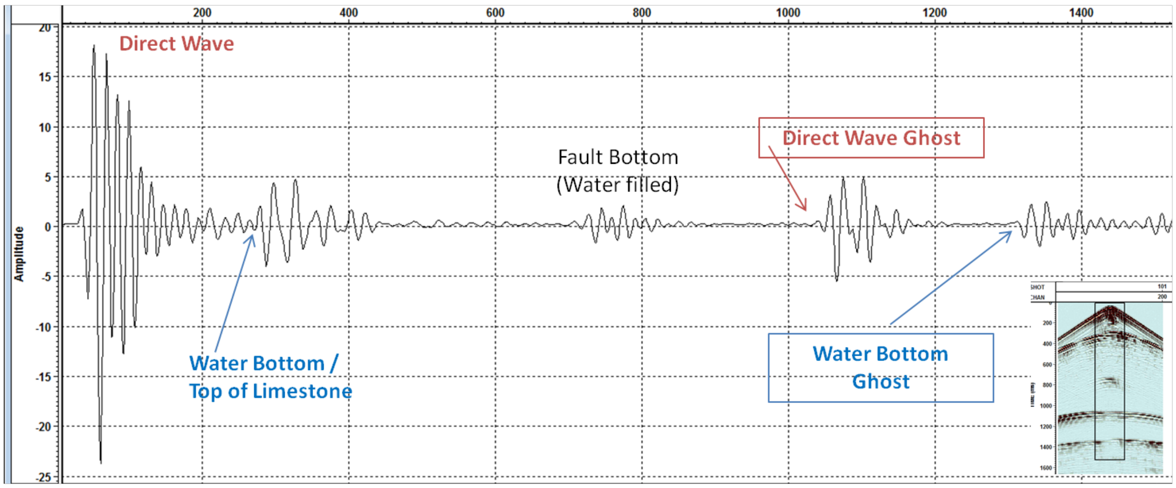

FIG. 22. Average trace calculation showing identified reflection events in the shot record. The traces calculated in the average are shown in the inset figure.

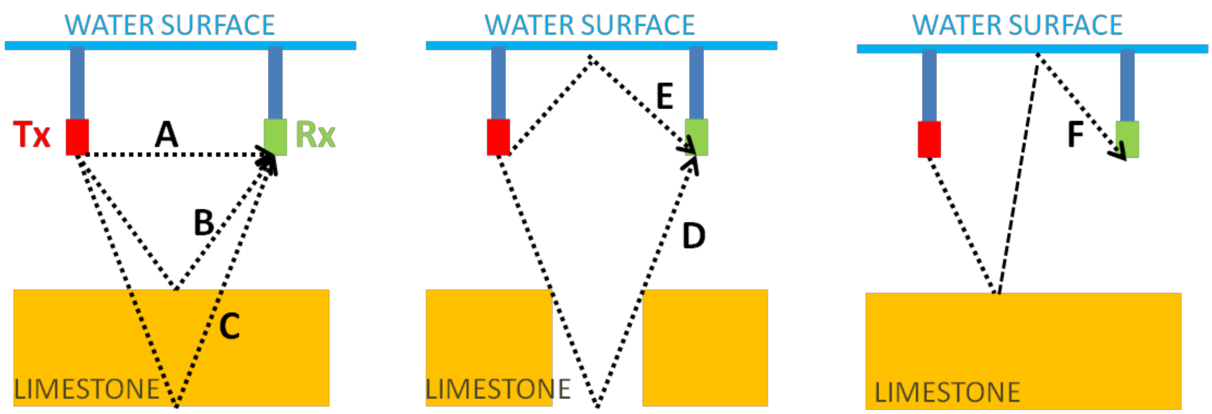

FIG. 23. Illustration of the events transmitted and received by the transducers. The ray paths taken through water and the model are used to calculate expected arrival time.

Table 2. Summary of expected two-way arrival times of the identified events.

LABEL	EVENT	EXPECTED 2-WAY TIME
A	Direct arrival	32 ms
B	Water bottom reflection	270 ms
C	Bottom of Limestone	390 ms
D	Water bottom of fault	670 – 720 ms
E	Source multiple (ghost)	~ 1080 ms
F	Receiver ghost	1290 ms

DISCUSSION

The final processed images of the Limestone model for a water filled and acrylic filled faults are compared in Figure 24. The surface of the 50 m fault with 10 m uplift is easily identified in all the images; however, the imaging quality of the deformation zone varies between the common-source and zero-offset data. Errors in velocity analysis of common-shot data can result in lower signal-to-noise in the stack, and mispositioning in migration. The constant velocity used for migrating the zero-offset data is limiting if complex structure is involved.

The bottom of the limestone is better resolved in the zero-offset sections. This is most likely due to difficulty in picking this event during velocity analysis. The water bottom of the fault is most apparent again, in the zero-offset section, at approximately 720 ms. The bottom of the acrylic fault is calculated to be close to 510 ms, and again, is imaged better in the zero-offset section.

All the images show what may be an event near 600 ms which was not previously discussed, and was not obvious in the shot domain of the common-source data. Ray tracing indicates that this event may be a result of peg leg reverberations in the limestone.

A 2D poststack time migrated seismic section of the New Zealand Greendale fault is shown in Figure 25. This seismic land data was collected by CREWES in April, 2011 and processed by Sensor Geophysical. A similar fault throw and wide fault zone is observed in both the physical modeled and field seismic sections.

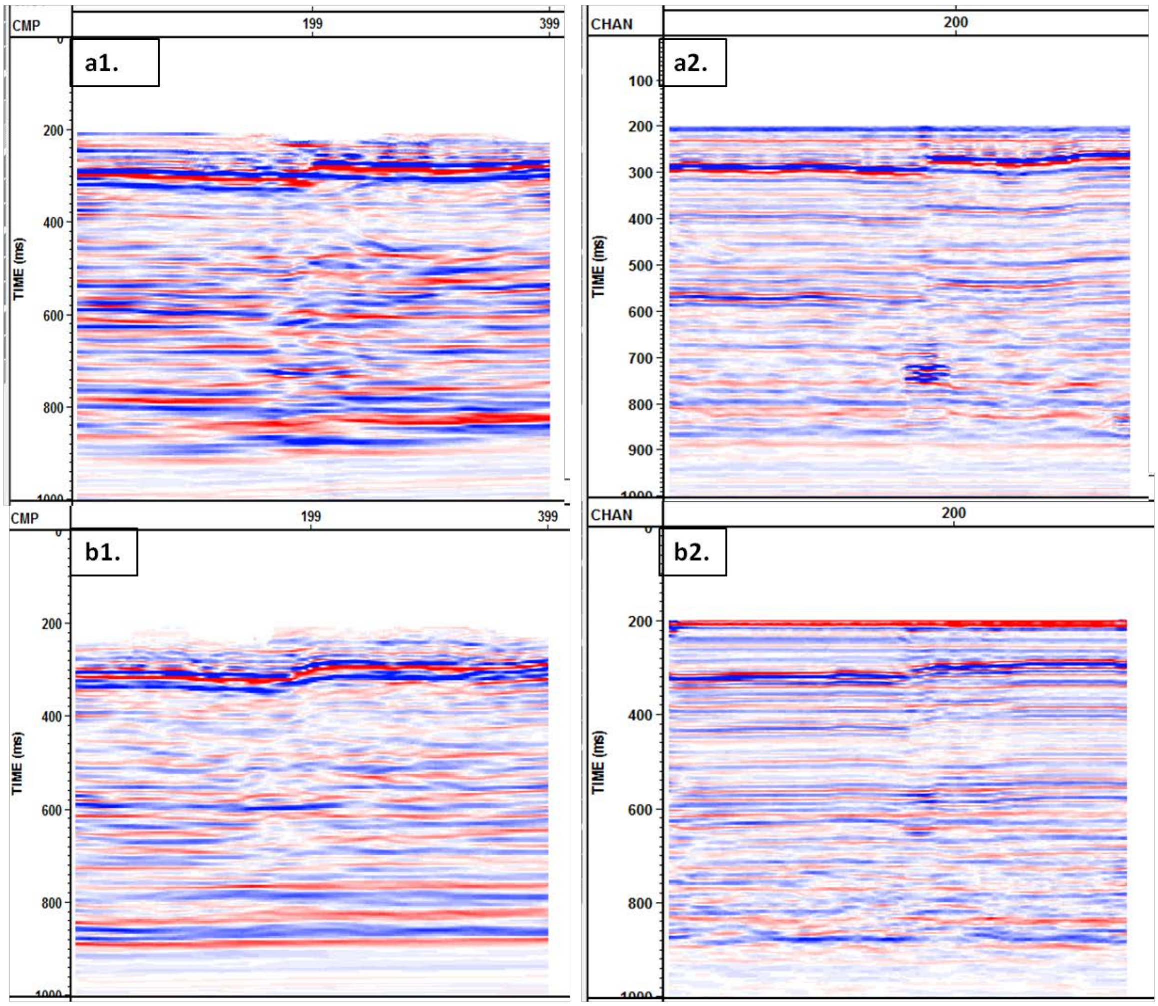

FIG. 24. Final postmigrated images of the modeled fault zone. a1) Common-source Limestone-Water fault model. a2) Zero-offset Limestone-Water fault model. b1) Common-source Limestone-Acrylic fault model. b2) Zero-offset Limestone-Acrylic fault model.

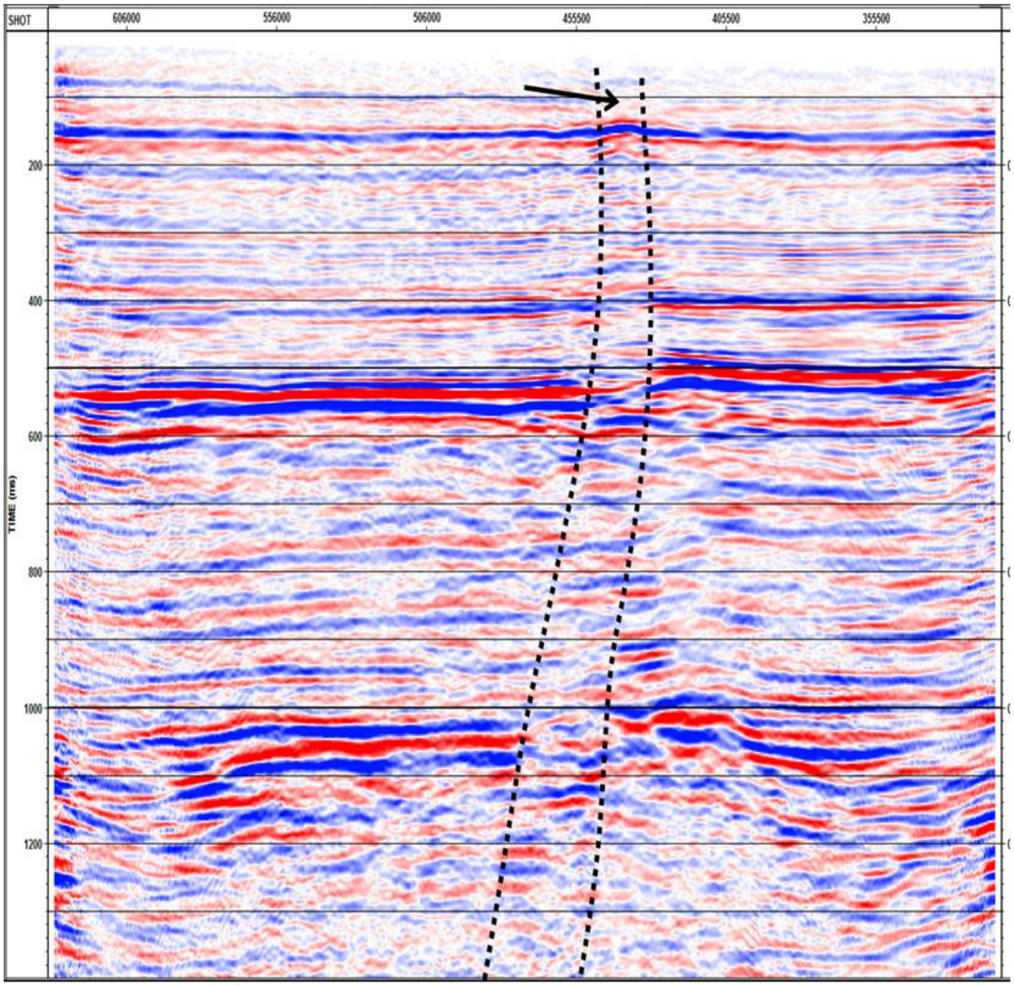

FIG 25. Post-stack migrated seismic section for the Greendale fault zone, new Zealand. The deformed fault zone is outlined.

CONCLUSIONS

Physical modeling provides a method to test seismic acquisition parameters for detecting fault resolvability. A great deal of consideration must be taken when designing a physical model to best represent a realistic geologic model. Selection of materials is important especially when considering attenuation, scaled geologic properties, and the ability to withstand long durations in water.

Processed model data yielded images that resolved a shallow fault with a small vertical throw and a deformed fault zone, similar to a field survey across a recent active fault in New Zealand. Resolution of seismic data is controlled not only by bandwidth, but acquisition and data processing parameters as well.

Now knowing the limitations of physical modeling, future work includes constructing a new model with a more complex fault deformation zone, and a greater depth. Numerical modeling would also be an asset to this project. As well, an interesting side topic which came to light in this project includes mirror imaging of the ghost reflections to better image the zone of interest.

ACKNOWLEDGMENTS

Thank you to Rick Arthur and Eric Gallant for helping create the physical models, and Malcolm Bertram, who was a great help with data geometry and initial processing. Thanks to GEDCO for use of VISTA seismic processing software. And finally, a sincere thank you to the CREWES sponsors for their support.

REFERENCES

Angona, F.A., 1960, Two-dimensional modeling and its application to seismic problems: Geophysics, 25, 468-482, doi: 10.1190/1.1438719.

Aydin, A., 2000, Fractures, faults, and hydrocarbon entrapment, migration and flow: Marine and Petroleum Geology, 12, 797-814, doi:10.1016/S0264-8172(00)00020-9.

Barnes, C., 1993, Instantaneous spectral bandwidth and dominant frequency with applications to seismic reflection data: Geophysics, 58, 419-428, doi: 10.1190/1.1443425.

Berg, R.R., and A.H. Avery, 1995, Sealing Properties of Tertiary Growth Faults, Texas Gulf Coast: AAPG Bulletin, 79, 3, 375-379.

Cheadle, S.P., M.B. Bertram, and D.C. Lawton, 1985, Development of a physical seismic modelling system, University of Calgary: Current research part A, Geological Survey of Canada, Paper no. 85-1A, 499-504.

Das, I., and M. Zoback, 2011, Long-period, long-duration seismic events during hydraulic fracture stimulation of a shale gas reservoir: The Leading Edge, 30, 7, 778–786, doi: 10.1190/1.3609093

Fossen, H., 2010, Structural Geology: Cambridge University Press.

French, W.S., 1974, Two-Dimensional and three-dimensional migration of model-experiment reflection profiles: Geophysics, 39, 265-277, doi: 10.1190/1.1440426.

Gallant, E.V., D.C. Lawton, and M.B. Bertram, 1991, Development of a physical modelling system for 3-C x 3-D experiments. CREWES Research Report, 33, 524-528.

Geldart, L.P., and R.E. Sheriff, 2004, Problems in Exploration Seismology and their solutions: Society of Exploration Geophysicists, p. 332.

Grion, S., E. Russell , M. Manin, X. Miao, A. Pica, Y. Wang, P. Granger, and S. Ronen, 2007, Mirror imaging of OBS data, First Break, 25, 37-42, doi:10.3997/1365-2397.2007028.

Hennings, P., P. Allwardt, P. Pijush, C. Zahm, R. Reid, H. Alley, R. Kirschner, B. Lee, and E. Hough, 2012, Relationship between fractures, fault zones, stress, and reservoir productivity in the Suban gas field, Sumatra, Indonesia: AAPG Bulletin, 96, 4, 753-772, doi: 10.1306/08161109084.

Hilterman, F.J., 1970, Three-dimensional seismic modeling: Geophysics, 35, 1020-1037, doi: 10.1190/1.1440140.

Kaiser , A.E., H. Horstmeyer, A.G. Green, F.M. Campbell, R.M. Langridge, and A.F. McClymony, 2011, Detailed images of the shallow Alpine Fault Zone, New Zealand, determined from narrow-azimuth 3D seismic reflection data: Geophysics, 70, no. 1, B19-B31, doi: 10.1190/1.3515920.

Lawton, D.C., S.P. Cheadle, E.V. Gallant, and M.B. Bertram, 1989, Elastic physical modeling, CREWES Research Report, 19, 273-288.

Lawton, D.C., G.F. Margrave, and E.V. Gallant, 1998, Physical modeling of an anisotropic thrust, CREWES Research Report, 10, no. 15, 1-9.

Lindsey, J., 1989, The Fresnel zone and its interpretative significance: The Leading Edge, 8, 33–39, doi: 10.1190/1.1439575.

Mooney, W.D., and A. Ginzburg, 1986, Seismic measurements of the internal properties of fault zones: Pure and Applied Geophyics, 124, 141-157, doi: 10.1007/BF00875723.

Sheriff, R.E., 1991, Encyclopedic Dictionary of Exploration Geophysics: Society of Exploration Geophysicists, p. 269.

Sun, S., and J.C. Bancroft, 2001, How much does the migration aperture actually contribute to the migration result?, CREWES Research Report 2001, 37.

Tamagawa, T., and D.D. Pollard, 2008, Fracture permeability created by perturbed stress fields around active faults in a fractured basement reservoir: AAPG Bulletin, 92, 6, 743-764, doi:10.1306/02050807013

Van Dissen, R., D. Barrell, N. Litchfield, P. Villamor, M. Quigley, A. King, K. Furlong, J. Begg, D. Townsend, H. Mackenzie, T. Stahl, D. Noble, B. Duffy, E. Bilderback, J. Claridge, A. Klahn, R. Jongens, S. Cox, R. Langridge, W. Ries, R. Dhakal, A. Smith, S. Horblow, R. Nicol, K. Pedley, H. Henham, R. Hunter, A. Zajac, and T. Mote, 2011. Surface rupture displacement on the Greendale Fault during the Mw 7.1 Darfield (Canterbury) earthquake, New Zealand, and its impact on man-made structures. In: Ninth Pacific Conference on Earthquake Engineering: Building an Earthquake-Resilient Society, Auckland, New Zealand 14-16 Apr 2011. Accessed 9 October 2011; http://db.nzsee.org.nz/2011/186.pdf.

Vermylen, J.P., and M.D. Zoback, 2011, Hydraulic fracturing, microseismic magnitudes, and stress evolution in the Barnett shale, Texas, USA: SPE 140507. SPE Hydraulic Fracturing Technology Conference and Exhibition. 24-26 January 2011. Texas, USA.

Wang, X., C. Xia, and X. Liu, 2012, A case study: imaging OBS multiples of South China Sea, Marine Geophysical Research, 33, 1, 89-95, doi:10.1007/s11001-012-9148-2.

Widess, M.B., 1973, How thin is a thin bed?: Geophysics, 38, 1176-1180, doi: 10.1190/1.1440403.

Wong, J., R. Maier, E. Gallant, and D. Lawton, 2009a, Physical modeling of a 3D marine seismic survey, CREWES Research Report, 21, 1-10.

Wong, J., Hall, K.W., Gallant, E.V., Maier, R., Bertram, M.B., Lawton, D.C., 2009b, Seismic Physical Modelling at the University of Calgary, CSEG Recorder, 34, p. 37-43.

Wong J., F. Mahmoudian, and G. Margrave, 2011, Physical modeling III: acquiring modeled data for VVAZ/AVAZ analysis, CREWES Research Report, 23, 1-17.

Yilmaz, O., 1987, Seismic data processing: Society of Exploration Geophysicists.

Zoback, M.D., A. Kohli, I. Das, and M. McClure, 2012, The importance of slow slip on faults during hydraulic fracturing stimulation of shale gas reservoirs: SPE 155476, SPE Americas Unconventional Resources Conference, 5-7 June 2012. Pittsburgh, Pennsylvania, USA